7. Cratering on Mars

Impact cratering is one of the fundamental geological processes, and is visible on every solid surface body in the solar system (e.g. Alfred Wegener, 1921). When the disrupted comet Shoemaker–Levi–9 hit Jupiter, it was the only and the most spectacular opportunity to observe an impact event, but it left just short–term turbulences in the Jovian atmosphere. On solid surfaces the impacting projectiles form bowl–shaped depressions, which are named craters after a certain type of ancient Greek vase. Depending on the impacting energy the crater morphology changes with diameter. This progression was already described by Gilbert in 1893.

Mariner 9 images have revealed a diverse range of morphology and ejecta characteristics and potential target differences (Arvidson *et al.*, 1976; McCauley, 1973). Impact crater morphology and especially ejecta are largely unique to Mars (although they are found on the jovian moon Europa and on Earth). They have probably been strongly influenced by subsurface volatiles and are widespread throughout the surface of the planet. The Martian impact record in terms of crater morphology, morphometry, modification and crater frequency has been catalogued by Strom *et al.* (1992), but their study also revealed the difficulties in the fundamental morphologic classification. Keys to explaining the large variety of central crater structures or ejecta blankets include the geological conditions of the surface and subsurface (possibly the atmosphere as well). The dependence of crater diameter on the condition of impacts, defined by the impacting body (radius, mass, density, impact velocity) and the planetary surface (surface gravity, density, strength) is generally estimated by a form of scaling that employs both theory and small scale measurements to extrapolate to the large scales of observed craters and impact basins (Holsapple, 1987; Holsapple and Schmidt, 1987; Schmidt and Housen, 1987; Croft, 1985b,a; O'Keefe and Ahrens, 1981). The cratering process is controlled by the target strength and for larger impacting bodies by the surface gravity (Schmidt and Housen, 1987). The final crater diameter and appearance depends on gravity and material parameters (Croft, 1985b,a). Besides the knowledge of impact mechanism, other obvious differences in the impact environment influences the final crater form, i.e. surface gravity, impact velocity, the presence of atmosphere and the probable abundance of water or ice in the Martian subsurface.

7.1. Cratering Mechanics

Independent of the final crater size, the process of impact cratering always follows a three stage scheme, which has been described in detail by Melosh (1989). The three stages of the impact cratering process are (1) contact and compression, (2) excavation, and (3) modification (Fig. 7.1).

During the first stage, the projectile contacts the target. As it hits, the target is instantaneously compressed and accelerated, while the projectile itself is decelerated by the resistance of the target. A shock wave originates at the point of contact and travels through target and projectile, producing pressures much larger than the yield strength of either the target or the projectile. This stage, lasting a "blink of an eye", ends after the shock wave has passed.

The second stage is divided into the expansion of the shock wave and the excavation flow. While the shock wave expands hemispherically (and subsequently degrades to a stress wave), the target material is set into motion radially away from the impact site (immediately behind the shock wave). Rarefaction waves create an upward–directed pressure gradient behind the

shock wave. This additional upward component to the radial velocity initializes the excavation flow and the largest portion of material ejects from the crater. This ejected material follows purely ballistic trajectories, the ejecta curtain. Material ejected first, closest to the impact site, has the highest velocities, and consequently takes the longest to fall. The growth of a crater up to the transient cavity starts as a hemispherical expansion following the shock wave until the final depth is achieved. Due to less resistance at the surface the crater diameter continues to grow further until its final diameter is achieved (Fig. 7.1). This state of the crater is called transient cavity. The final observed rim–to–rim diameter is different from the transient diameter and is reached in the last, so–called modification stage.

During the final modification stage, the ejected debris is finally deposited and the crater interior becomes modified. The fundamental idea of ejecta emplacement is that the ejected material travels in a near parabolic trajectory as a so–called ejecta curtain (ballistically). Based on observations, one expects very little material to escape the gravitational field of a planet, most falling back to the surface and forming a continuous ejecta blanket surrounding the crater. The innermost ejecta are launched first, travel fastest and can reach long distances. Ejecta originating farther from the center are launched later, moving more slowly and falling sooner and closer to the rim. Only material from the uppermost third to half of the depth of the transient crater is excavated from the crater. Target material deeper than the maximum excavation depth has been displaced beneath the crater floor. The maximum excavation depth (and the strata represented in the ejecta blanket) is considerably shallower than the maximum crater depth. Close to the rim, material is deposited in reversed original stratigraphy (overturned flap, Roddy *et al.* (1975)). The continuous ejecta blanket covers an area of roughly one crater radius from the crater rim, followed by a thin and patchy unit. In the latter unit and beyond, secondary craters

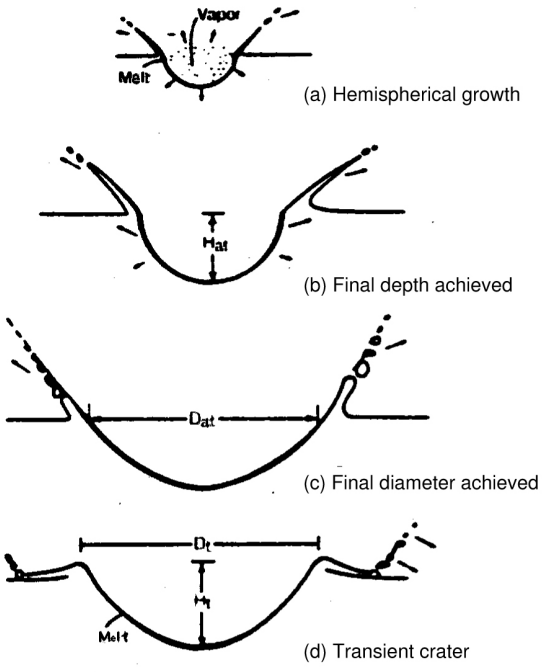

Figure 7.1.: The growth of a crater: The crater first opens following the hemispherical expansion of the shock wave (a). The growth rate is steadily decreasing due to the resistance of the underlying target rocks until its maximum depth is achieved (b). Less resistance at surface let the crater diameter continue to grow (c) and stops when no more material is ejected. The resulting transient crater is broader than a hemisphere (d) (Fig. from Melosh (1989)). Depending of the size of the transient crater, modification in the given gravity field results in different morphologies.

can be found, which are formed by large chunks of material during the excavation period. On the Moon, secondary craters can reach a size of about 4% the diameter of the primary impact crater. The secondary crater itself is not necessarily distinguishable on the basis of its morphology (they could appear more elliptical), but ejecta of secondaries have a characteristic V–shaped ridge pointing radially away from the main crater. Cluster or chain formation also help to identify them. Lined up as a chain, the chevron pattern turns into a herringbone pattern (Oberbeck and Morrison, 1973). In gen-

eral, these crater–field forms are all strongly controlled by the gravity field of the planet.

The change of the crater interior during the modification stage varies, depending upon the size of the transient cavity, and the shape characteristic of simple or progressively complex impact craters. For small craters, forming a final simple bowl–shaped crater, the transient cavity is filled by material falling back from the unstable rim to subsequently fill the center of the crater (wall slumping, Moore (1976)). The larger an impact crater, the further the initial transient departs from gravitational stability and is modified more strongly during this last crater forming stage.

7.2. Crater Modeling

Currently, the applied crater size–frequency distribution is based on the transferred lunar curve. This transfer procedure is outlined in Section 5 and discussed in detail by Neukum and Ivanov (1994); Ivanov (2001). To further refine and verify the modeling and transfer of the Martian crater production function, pre–existing modeling efforts have been continued by refining existing scaling laws, improving models for crater collapse, and estimating the impacting flux of planetesimals, including comets (Ivanov, 2001). Target parameters such as subsurface water, sedimentary and volcanic rocks of different water or ice saturation stages lead to a variety of scenarios that influence the final crater diameter, and therefore deviate from the analytical Martian crater size–frequency distribution. Measurements and analogue modeling of the crater size–frequency distribution on different geological units might be a key to understand the influence of target properties in Martian conditions.

Remote sensing combined with geological and geophysical investigations on Earth provide boundary conditions and "ground–truth" data sets of surface and subsurface morphology for crater modeling. Laboratory experiments and studies of nuclear explosions form the basis for the understanding of the dynamic behavior of the impact cratering event. These experiments are limited in reproducing the effects of high–energy impacts, which involve extreme pressures, temperatures and large crater–diameter range (role of gravity during the formation of large craters). Therefore, computer simulations are the only feasible method to study large–scale impact events. The complexity of the process involved during the crater formation, especially the passage of shock waves and the irreversible behavior of geologic material are translated into computer codes that handle the shock wave propagation (velocities, stresses and strains) as a function of time and position. These are called hydrodynamical computer codes ("hydrocodes"). These codes are based on a discretized particle motion established through the principles of conservation of momentum, mass and energy from a macroscopic point of view (Anderson, 1987), the equation–of–state, relating pressure, density and the specific internal energy (needed to describe compressibility effects and irreversible thermodynamic processes), and a rheology (constitutive) model, which describes the response of a material to deformation (change in shape or strength properties).

One of the most important issues concerning hydrocodes is the description of the discontinuous nature of shock waves, which may introduce instabilities in the discretized representation. The choice of a discretization approach and solving methods depends on the problem to be solved, so a variety of hydrocodes have been developed. An additional difficulty, besides the description of the problem itself, is the equation of state of the geologic material investigated. The crater modeling is an iterative process comparing observations and modelling results.

7.3. Impact Crater Morphologies

A variety of morphology-based classification and description schemes have been proposed to describe the wide range of observed crater and ejecta morphologies. Following Dence (1965),

craters are classified as *Simple* and progressively more *Complex* craters:

Simple Craters appear as bowl-shaped circular depressions, with raised rims and approximately parabolic interior cross sections. The inner walls, close to the angle of repose, can be modified due to gravity–driven erosional processes. For lunar craters, Pike (1977) estimated a depth–to–diameter ratio near 1 : 5. Comparison between planets show that the transition diameter between simple and complex craters (see below) is dominantly inversely related to surface gravity, but also to target properties. This transition is on the Moon at diameters around 15 km, on Mars about 7 km, and on Earth depending on the target rock, between 3 to 5 km (for sedimentary or crystalline rocks). Investigations on Earth indicated that the apparent crater is filled roughly to half of its real depth by a lens of broken and shock–melted rocks (Grieve *et al.*, 1977). The mechanical process to generate simple craters is essentially that of the gravitational collapse of the rim of the transient crater cavity.

Complex Craters: Craters reaching the "transition diameter" have a more complex interior. Their rim is more synclined, the craters are surrounded by circular faults and in their interior a central structural uplift is developed. With increasing diameter they show single or multiple central peaks, flat floors and terraced rims. When compared to simple craters, the depth of complex craters increases less with increasing diameter. If the craters grow larger, the central peak evolves to an inner mountain ring. Again, there seems to be a 1/g scaling for the transition diameter.

Multi–Ring Basins: These are the largest, most complex impact craters and show multiple rings. One typical example is the lunar Orientale basin. It possesses at least five circular rings forming inward facing scarps of up to 6 km in height. On icy targets they look slightly different, but they are considered to originate as a tectonic response of the icy and rocky lithosphere to the impact cavity (Melosh and McKinnon, 1978; McKinnon and Melosh, 1980). In the case of Mars, due to strong erosional degradation of the largest basins (Hellas, Argyre, Isidis) and filling, one cannot judge whether or not there have been prominent ring features (Wood and Head, 1976). No gravity scaling could be found and ring separation is most likely dependent on the near-surface rheology.

Martian Special Crater Cases: Ejecta blankets of lunar craters are usually blocky near the rim, grading outward with increasingly more fine–grained particles until the blanket merges with the surrounding area. These features are consistent with the ballistic emplacement of the ejecta. Many Martian craters have ejecta deposits that appear to have flowed over the surrounding surface like mud-flows. These craters are known as rampart, fluidized, or splash craters. Their ejecta consist of several relatively thin sheets with tongue-shaped fronts, while a ridge formed at the front of each ejecta lobe. Numerous characteristics of the Ries Crater (Germany) show similarities to craters on Mars, indicating that Martian fluidized ejecta craters may be closer analogs to this terrestrial crater than lunar craters (Mouginis-Mark, 1981). Geologic evidence indicates that the Martian surface has been substantially modified by the action of water and that much of the water still resides beneath the surface as ground ice. In particular, the fluid appearance of rampart crater ejecta has been cited as evidence for subsurface ice at the time of impact. If this interpretation is correct, then the size–frequency distribution of rampart craters broadly consists with the depth distribution of ice, inferred from stability calculations. Ejecta morphology has proven to be a useful tool for studying the distribution of subsurface ice on Mars (e.g. Kuz'min *et al.*, 1989).

7.4. Crater Morphologies: Indicators of Sub–Surface Water

Morphologies of differently sized craters superimposed on variuos geological units allow us to

assess the role of the projectile nature and target properties (e.g. water or ice content) in the crater formation process and thus in the morphological appearance and size parameters of craters (if compared to numerical model results).

Structures/Landforms that may reflect volatile content include craters with fluidized ejecta blankets (FEB, Gault and Greeley, 1978). Schultz and Gault (1979) suggested the atmosphere affected the Martian ejecta emplacement. Barlow and Perez (2003) correlated the occurence of FEBs with the proposed locations of near–surface water/ice as detected by Mars Odyssey (Mitrofanov *et al.*, 2002; Feldman *et al.*, 2002). Craters vary in terms of their interior morphology and some quantitative parameters, including crater depth/diameter, rim height/diameter ratios and diameter ratios of crater cavities to their ejecta blankets. It is widely believed that FEBs indicate the presence of water or ice in the subsurface at the time of impact. Comparing crater morphology and morphometry for various FEB appearances may provide us with a key to understanding both the amount of volatiles in the target as well as crater–scaling laws and, finally, improve the absolute Mars cratering chronology transferred from the Moon (see Chapter 5).

Large–crater morphology: Double–ring craters such as Lyot, Lowell, Kepler, Galle and Flaugergues, all roughly 200 to 250 km in diameter with ages between 3.9 Ga and 3.4 Ga (Chapter 13), were selected. The goal is to find/understand differences in the crater morphometry of large craters in various geologic regions of Mars.

They appear (if not filled by sediments, for example Kepler) as rather deep depressions with distinct inner ring features. Lyot, one of these craters situated in the south of the Northern Plains at the dichotomy boundary, was previously considered by Russell and Head (2002) as a crater whose transient cavity penetrated into the global aquifer suggested in the hydrology model of Mars by Clifford (1993). However, these authors did not find morphological evidence of the cavity penetrating to an aquifer and did not analyze Lyot in relation to the above mentioned morphometric parameters.

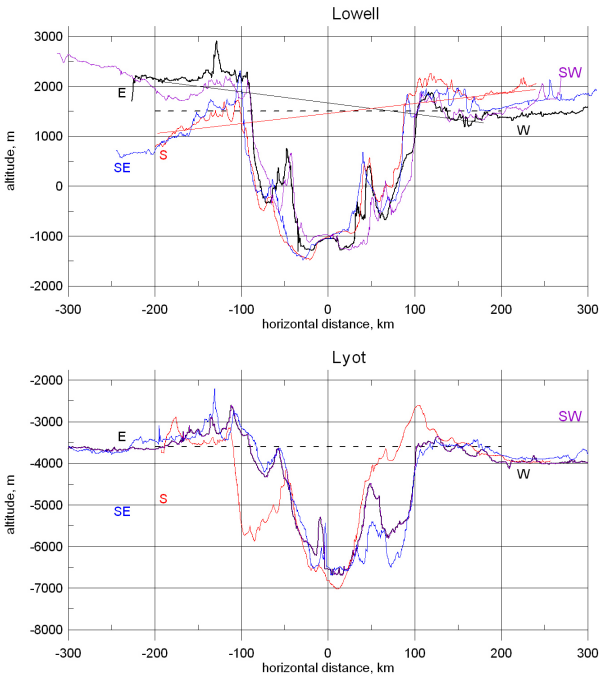

Figure 7.2.: Cross sections based on MOLA topographic data of impact crater Lowell (top) and Lyot (bottom). Lowell is an example for the highland units, while Lyot is the only large crater which could be representative for the lowland units. The main difference is the relative inner rim height when compared to a pre–impact surface level, for absolute values see Table 7.1; (Figure from Werner *et al.*, 2004a).

Morphometric characteristics derived from MOLA topographic data are compared in Table 7.1. Large variations in the maximum apparent depth are observed, yielding different levels of infill. Nevertheless, the apparent depth of the inner rim crest (measured from the pre–impact surface level) is situated about 1.5 km below the local pre–impact level for all craters except Lyot (Werner *et al.*, 2004a, see Fig. 7.2). The inner rim of Lyot reaches the pre–impact level. Considering that only Lyot is situated

in the Northern Lowland plains, this indicates that even for large craters some morphometric parameters may vary and reflect differences in the target properties.

Smaller–Crater Morphometry: Considering smaller and more numerous craters, a more representative result might be derived. We started with a set of craters with diameters of about 30 km. From Barlow's catalog we compiled 5 to 6 example craters for various morphologic classes: single, double, and multiple lobated, as well as appearingly "dry" crater ejecta blanket. In addition, several "unclassified" craters are investigated. The profiles for each crater were selected from MOLA topographic data for four cross sections through the crater center.

The more or less prominent central peak is a typical appearance of craters in that size range. Guided by the results of the large craters, we focused on a few of the main morphometric parameters: diameter, inner slope angle, rim height, and central peak position below the pre–impact surface level. The results are represented in Fig. 7.3. Crater depth is not considered, as many craters are partially filled by aeolian or other deposits. It appears that the central peak position below the pre–impact surface level and the average rim height are not in agreement with the expected change in target properties, as reflected in ejecta blanket morphology (Werner *et al.*, 2004a). The main difference found in the limited data test set is a weak tendency for craters with single lobe ejecta to have less steep inner walls (Werner *et al.*, 2004a). We also note the systematic deviation of measured parameters from the generalized relationships published by Garvin *et al.* (2003), Fig. 7.3).

Numerical modeling of impact cratering: Numerical modeling allows us to investigate how the crater size and morphology depends on the projectile impact velocity, target strength, etc. (Ivanov *et al.*, 1997). Modeling of the projectile–type influence (2–km diameter asteroid at 8 km/s vs. 2-km diameter comet at 15.5 km/s) on the crater diameter and depth did not yield any significant difference in the crater diameter (about 30 km), depth (1 km) and inner slope steepness (about 15°). However, the impact melt production and central peak morphology were found to differ (Fig. 7.4).

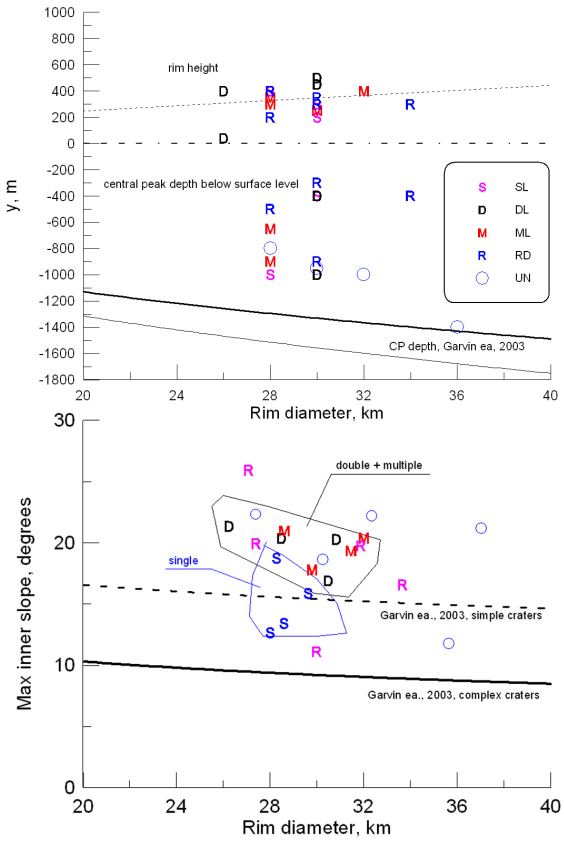

Figure 7.3.: TOP: Rim heights and central peak (CP) depth below the initial target level for craters with various types of ejecta blanket: single (SL), double (DL) and multi-(ML) lobed , radial ("dry") deposites (RD), and unclassified cases (UN). All data for CP depth are well above averaged relationships by Garvin et al. (2003). BOTTOM: Maximum slope for the same craters as in Fig.2. Craters with SL ejecta tend to have less steep maximum slope of inner walls. All data are well above the average relationships from Garvin et al (2003); (Figure assembled and provided by B. A. Ivanov; from Werner *et al.*, 2004a).

We have compared our results with observational data from Garvin *et al.* (2003) and found

Martian Small–Basin Morphology

	Diameter D km	Max. apparent depth h m	Apparent depth of inner rim crest m	Pre–impact altitude (estim.) m	Visible State
Kepler	233	1200	800	+2300	partially filled
Lowell	203	3000	1000	+1500	partially filled
Galle	230	2900	1500	–300	partially filled
Secchi	234	1900	1300	+2200	partially filled
Flaugergues	245	1100	>1100	+150	heavily filled
Lyot	236	3400	200	–3600	lightly filled

Table 7.1.: The dimensions of small Martian basins indicate a difference between highland craters and Lyot, which is situtated at the dichotomy boundary and could be representative for the lowland units. The only difference found is the inner–rim height below the pre–impact surface level (see Fig. 7.2).

a good fit for the crater depth, rim height and central mound width, but a poor fit for the central peak height, i.e. the computed peak was too high.

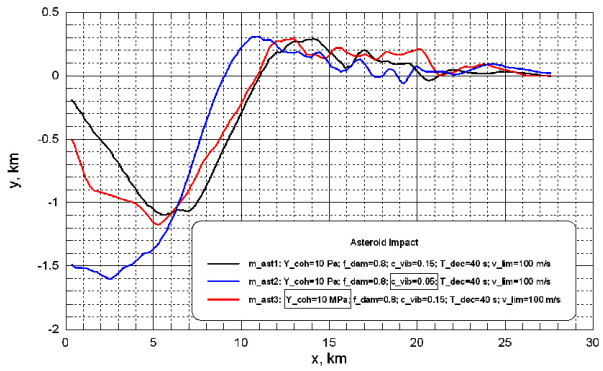

Figure 7.4.: Crater profiles from numerical modeling of a vertical asteroid impact (projectile diameter of 2 km at impact velocity of 8 km s^{-1}). The starting run (black curve) produced a crater with a 28 km rim–crest diameter and central peak uplifted about 200 m below the pre–impact surface. Changes in the model parameters (intensity of the acoustic–fluidization model block oscillations - red curve - or the cohesion of damaged material - blue curve) result in a crater shape with smaller diameter and less developed central peak (Modeling results provided by B. A. Ivanov, 2004)

Nevertheless, modeling the morphologic and morphometric characteristics of these craters gives us sets of model parameters, such as target strength, and a key to understanding the influence of water in the target on the crater morphology and the mobility of ejecta. Comparison with the numerical model of a similarly sized crater shows that the model with the initial set of parameters allows us to reproduce the general crater morphology (central peak crater) and crater depth. The variation of the model parameters can be used to understand the dependence of the crater shape on material properties of a target. Figure 7.4 shows three model runs, where the parameters describing either the intensity of the acoustic–fluidization model block oscillations or the cohesion of damaged material are varied. Decreasing the intensity or increasing the cohesion results in a crater shape with smaller diameter and less developed central peak. Both parameters act on the crater collapse process during crater modification, forcing the movement (central peak rising) to stop earlier for a given initial shear stress.

Slope measurements: We continued our initial attempt to understand target properties, reflected in the resulting crater morphology, by investigating the inner slope angles. We have found a weak tendency (see above) which we try to confirm. Following the findings that inner slope characteristics are dependent on the projectile or target properties, a detailed study of slope angles in different geologic units as well as at different latitudes was undertaken.

In addition to new digital terrain models derived from HRSC imagery, we used THEMIS and HRSC imagery of comparable resolution as well as MOLA topographic information where HRSC data were unavailable.

For the slope measurements, we extracted profiles from track–based MOLA and image–based HRSC topographic data. The slope angles are derived from a linear fit based on a moving–window of about 4 to 5 points, which is equivalent to a baseline of about 1 km. We looked for the maximum slope on each profile and determined the maximum slope angle averaged for all profiles (summarized in Fig. 7.5). The crater diameters of the investigated craters range between 5 km to 70 km. Individual terraces in the inner crater walls were investigated separately. In addition to crater walls, plateau and caldera walls were studied in this way. All measurements are based on imagery from very early on the HRSC mission, and are scattered in the equatorial zone. The comparison of MOLA and HRSC digital terrain models shows no significant differences between the two datasets (within the error bars and not considering systematic shifts or tilts). A slightly underestimated slope angle is observed due to the large footprint of the individual measurement that averages more than the imagery–based HRSC topographic data.

The measured slopes appear to be diameter independent (not as suspected above) and around 28°, indicating a friction coefficient k = 0.53 on a base of 1 km (compare Fig. 7.5, red stars and pink E). A clear difference between highland and lowland material is not observed.

Comparing slope measurements based on MOLA in the equatorial and polar regions of Mars (compare Fig. 7.5, blue P), a different situation appears: the approximate 18° slope angles indicate less steep walls (indicating a friction coefficient k = 0.32 on a base of 1 km). In the polar region, a lower friction is possibly observed. Similar observations have been made by Kreslavsky and Head (2000) and they found a latitudinal change in surface roughness/smoothness (measured in wave length and slope angles) going northward towards smoother regions.

The difference between the polar and mid–latitude to equator crater slopes observed here could signify a difference in the upper crust material between polar and "continental" material, indicating a lower friction. The angle of repose measured for the polar region is less than 20° and between 30° and 40° elsewhere, and could be due to lower cohesion and the presence of water. While we could not correlate slopes to geological units (suggesting different target properties), variations with latitude is seen. In polar regions, observed craters appear to have less steep inner walls than in equatorial regions.

When comparing our slope measurements to a global dataset by Kreslavsky and Head (2000), a similar latitudinal dependency is observed. A general decrease in surface roughness towards the poles does not necessarily reveal a crater formation related effect and must be tested carefully. The presence of water or ice in the subsurface has been heavily discussed. It is unclear whether two competing processes result in larger or smaller craters. The presence of ice could cement and strengthen the target material (resulting in a smaller crater, T. Ahrens, 2004, pers. comm.) or increase the explosive nature of the formation (resulting in a larger crater, B.A. Ivanov, 2004, pers. comm.). Nevertheless, the results both from modeling and geologic target diversity were inconclusively in determining if the difference in inner slope angles is due to the impact cratering process in a target containing ice, or due to subsequent modification processes. In carfully examining the results of Kreslavsky and Head (2000), we found that fresh–looking craters in the polar region have steep slopes similar to those at the equator. Nine craters, with diameter larger than 5 km in the northern latitudes between the polar deposits and 60° N, are highly sampled by MOLA–tracks and show steep walls (more than 35° at 300 m–baseline). Almost everywhere, only the N–facing wall is

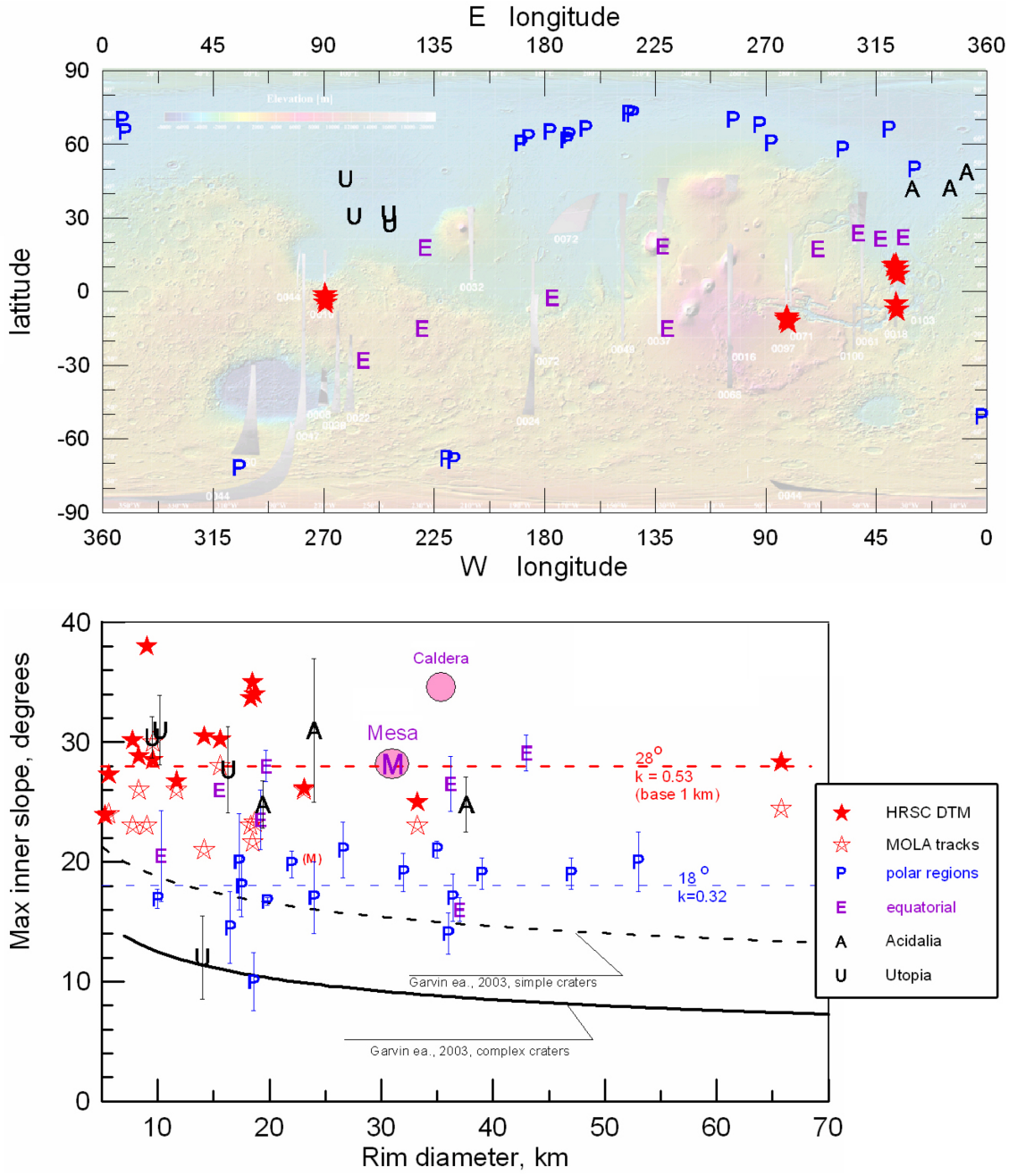

Figure 7.5.: Measurements of the slope of the inner crater rim, for details compare the text. (Figure assembled and provided by B. A. Ivanov, 2004).

steep (M.A. Kreslavsky, 2004, pers. comm.). It is likely that the general and detailed view of slope angles for craters studied here is related to post–formation processes, obscuring any cratering related observations.

Conclusion: Evidently, craters in the gravity–controlled regime do not show target related variations that might obscure the measurable crater size–frequency distribution for different geological units, and therefore, the crater count–based ages.